

Endmember selection for multiple endmember spectral mixture analysis using endmember average RMSE

Philip E. Dennison*, Dar A. Roberts

Department of Geography, University of California Santa Barbara, Santa Barbara, CA EH3611, USA

Received 27 January 2003; received in revised form 5 May 2003; accepted 29 May 2003

Abstract

Multiple endmember spectral mixture analysis (MESMA) models mixed spectra as a linear combination of endmembers that are allowed to vary in number and type on a per pixel basis. For modeling an image using MESMA, a parsimonious set of endmembers is desirable for computational efficiency and operational simplicity. This paper presents a method of selecting endmembers from a spectral library for use in MESMA. Endmember average root mean square error (EAR) uses MESMA to determine the average error of an endmember modeling spectra within its land cover class. The minimum EAR endmember is the most representative endmember for a land cover class within the spectral library and can be used to model the larger image.

These techniques were used to map land cover, including four dominant vegetation species, soil, and senesced grass, in the Santa Ynez Mountains above Santa Barbara, CA, USA. Image spectra were extracted from a 20-m resolution airborne visible infrared imaging spectrometer (AVIRIS) reflectance image using reference polygons and combined into a library of 915 spectra. Possible confusion between land cover classes was determined using the class average RMSE (CAR). EAR was used to select the single most representative endmember within each land cover class. The six minimum EAR endmembers were used to map the AVIRIS image. Land cover class accuracy was assessed at 88.6%. Using a fractional accuracy assessment, undermodeling of dominant land cover classes and overmodeling of absent land cover classes was found at the pixel scale. Land cover mapped using the minimum EAR endmembers represents a substantial improvement in accuracy over previous efforts.

© 2003 Elsevier Inc. All rights reserved.

Keywords: Imaging spectroscopy; Spectral mixture analysis; Endmember selection; Vegetation mapping

1. Introduction

A spectrum measured by a sensor is the combination of the spectra of the materials within the sensor's field of view. This spectral mixing occurs at all scales, from the microscopic scale of mineral grains, where mixing is typically non-linear, to kilometer scale land cover. Spectral mixture analysis (SMA), a technique based on modeling image spectra as the linear combination of endmembers, has been used to derive the fractional contribution of endmember materials to image spectra in a wide variety of applications. SMA has been extensively applied to the characterization of surface materials on the Moon and Mars (Adams, Smith, & Gillespie, 1986; Bell, Farrand, Johnson, & Morris, 2002;

Mustard & Head, 1996; Pinet, Shevchenko, Chevrel, Daydou, & Rosemberg, 2000). SMA has also been used in applications as diverse as monitoring urban environments (Phinn, Stanford, Scarth, Murray, & Shyy, 2002; Small, 2002), measuring water turbidity (Kameyama, Yamagata, Nakamura, & Kaneko, 2001), and mapping land degradation (Haboudane, Bonn, Royer, Sommer, & Mehl, 2002; Metternicht & Fermont, 1998). SMA has become an essential tool for remote sensing vegetation analysis. Since SMA can be used to provide a full spectrum measurement of vegetation response, SMA fractions are more robust than traditional vegetation indices (Elmore, Mustard, Manning, & Lobell, 2000; Peddle, Brunke, & Hall, 2001; Riano et al., 2002). Fractions modeled by SMA have been linked to vegetation biophysical parameters in boreal forest and savannah ecosystems (Asner, Bateson, Privette, Elsaleous, & Wessman, 1998; Hall, Shimabukuro, & Huemmrich, 1995; Peddle et al., 2001; Peddle, Hall, & LeDrew, 1999). Vegetation fractions produced by SMA have been used to

* Corresponding author. Tel.: +1-805-893-4434; fax: +1-805-893-3146.

E-mail address: dennison@geog.ucsb.edu (P.E. Dennison).

describe fractional vegetation cover (e.g. Cross, Settle, Drake, & Paivinen, 1991), land cover change (Elmore et al., 2000; Roberts et al., 2002; Rogan, Franklin, & Roberts, 2002), seasonal changes in vegetation (Roberts, Green, & Adams, 1997; Garcia & Ustin, 2001), and regeneration after disturbance (Riano et al., 2002).

Roberts et al. (1998) introduced multiple endmember spectral mixture analysis (MESMA), a technique for identifying materials in a hyperspectral image using endmembers from a spectral library. MESMA has been applied in a variety of environments for vegetation and geological analysis. Roberts, Gardner, Church, Ustin, and Green (1997), Roberts et al. (1998, in press), and Dennison, Roberts, and Regelbrugge (2000) used MESMA to map vegetation species and land cover type in Southern California chaparral. Painter, Roberts, Green, and Dozier (1998) and Painter, Dozier, Roberts, Davis, and Green (2003) mapped snow grain size in the Sierra Nevada of California using a MESMA approach. MESMA has also been used to map lunar surface composition (Li & Mustard, in press) and vegetation in semi-arid environments in California (Okin, Roberts, Murray, & Okin, 2001) and Namibia (Theseira, Thomas, & Sannier, 2002). This paper expands on these efforts by providing a method for selecting the most representative endmember of a land cover class from a spectral library using MESMA. The selected endmembers were used to map vegetation species and fractional cover from an AVIRIS image, and the accuracies of the mapped variables were assessed.

2. Background

SMA is a model based on the linear mixing of two or more “pure” spectral endmembers (Adams et al., 1993). SMA allows for variability in composition and illumination within an image. Image pixels (spectra measured within the instantaneous field of view) are modeled as the linear mixture of the endmembers, and a shade endmember is used to account for variation in illumination. One or more non-shade endmembers represent different materials within the image. Endmembers can be selected from image pixels, measured in the field or laboratory, or even created as “virtual” endmembers (Adams et al., 1993; Gillespie et al., 1990; Tompkins, Mustard, Pieters, & Forsyth, 1997).

In SMA, the reflectance of a pixel (ρ'_λ) is determined by the sum of the reflectance of each material within a pixel multiplied by its fractional cover:

$$\rho'_\lambda = \sum_{i=1}^N f_i \rho_{i\lambda} + \varepsilon_\lambda \quad (1)$$

where $\rho_{i\lambda}$ is the reflectance of endmember i for a specific band (λ), f_i is the fraction of the endmember, N is the number of endmembers, and ε_λ is the residual error. The

modeled fractions of the endmembers are commonly constrained by:

$$\sum_{i=1}^N f_i = 1 \quad (2)$$

Model fit is assessed using the model residuals (ε_λ) or the root mean squared error (RMSE):

$$\text{RMSE} = \sqrt{\frac{\sum_{\lambda=1}^M (\varepsilon_\lambda)^2}{M}} \quad (3)$$

where M is the number of bands. SMA typically assumes single interactions between photons and surfaces, producing linear mixing of the surface fractions and their reflectances. Non-linear mixing due to multiple scattering by vegetation canopies or vegetation and soil surfaces can become significant (Borel & Gerstl, 1994; Huete, 1986; Ray & Murray, 1996; Roberts, Smith, & Adams, 1993). Inability to account for non-linear mixing is an acknowledged limitation of SMA (Adams et al., 1993). In line with the assumptions of SMA, this paper assumes mixing is linear.

Tompkins et al. (1997) point out that endmember selection is vital to SMA. To take advantage of the ability of SMA to provide a physically meaningful fraction, the selected endmembers must be carefully chosen. Various methods for selecting endmembers for SMA rely on choosing extreme endmembers. Smith, Johnson, and Adams (1985) used principal component analysis (PCA) on a library of mineral spectra. Endmembers were projected onto the principal axes of variation to determine their purity for modeling mineral mixtures. Bateson and Curtiss (1996) used PCA and multidimensional visualization software to select endmembers interactively. Boardman (1993) used a different approach, selecting image endmembers through the determination of a simplex that fits the image data. A convex shape that contains the image data is derived, and the vertices of the best fitting simplex are used as endmembers (Boardman, 1993). Boardman, Kruse, and Green (1995) developed a Pixel Purity Index (PPI) that can be used to select image endmembers. Pixels from the image are transformed and projected onto a random unit vector. The most extreme pixels are determined for each projection onto a random unit vector. The number of times the pixel is selected as extreme determines its PPI and pixels with high PPIs are selected as endmembers for the image (Boardman et al., 1995). Tompkins et al. introduced a modified SMA in which virtual endmembers are chosen to minimize RMSE within user-specified constraints. This approach permits the creation of endmembers that are “more pure” than potential endmembers from the image itself.

The endmembers used in SMA are the same for each pixel, regardless of whether the materials represented by the endmembers are present in the pixel. Uncommon materials, which may not merit their own endmember, may be poorly

modeled by SMA. SMA also does not account for spectral variations present within the same material, since it permits only one endmember per material. MESMA addresses these concerns by allowing endmembers to vary on a per-pixel basis (Roberts et al., 1998). Endmembers are selected from a regionally specific spectral library, which can contain image and/or reference spectra (Roberts, Dennison, Ustin, Reith, & Morais, 1999). Model fit is determined by three criteria: fraction, RMSE, and the residuals of contiguous bands (Roberts et al., 1998). The minimum RMSE model is assigned to each pixel, and can be used to map materials and fractions within the image (Painter et al., 1998). Since the number of possible materials in an image can be very large, and since MESMA permits multiple endmembers for each material, an appropriate spectral library could contain hundreds of spectra. Modeling a large number of spectra for each pixel reduces the computational efficiency of MESMA and complicates interpretation of the resulting image. Endmember selection is necessary to create a balance between the inclusiveness of the spectral library and computational efficiency (Okin et al., 2001).

Several endmember selection methods have been proposed for multiple endmember techniques. These methods have concentrated on finding the set of endmembers that best represents spectral variations of materials in an image. Painter et al. (1998) and Okin et al. (2001) used a limited number of reference spectra or a priori knowledge to select endmembers for their analyses. Roberts, Gardner, et al. (1997) devised a hierarchical endmember selection rule that classified endmembers as specialists or generalists based on their ability to model the spectra of other materials. Specialist endmembers were used to unmix the scene first; unmodeled pixels were then unmixed by more generalist endmembers. Roberts et al. (1998) addressed endmember selection as a maximal covering problem (Church & Reville, 1974). Endmembers were selected to maximize the area mapped and minimize the overlap between models. Bateson, Asner, and Wessman (2000) grew endmember “bundles” within a simplex containing the image spectra. The multiple endmembers within each bundle account for the spectral variation in endmember materials. Orthogonal projection and PCA have also been used to find suitable candidate endmembers for unmixing image spectra (Maselli, 1998, Pinet et al., 2000). This paper presents a new technique for selecting endmembers for MESMA by using the endmembers that best model the spectral library. The endmember with the minimum average RMSE within a class is selected as the most representative endmember for the class.

3. Methods

3.1. Study area

The airborne visible infrared imaging spectrometer (AVIRIS) data used in this study were collected over

the city of Santa Barbara, CA, USA and the southern slope of the Santa Ynez Mountains. The elevation within the study area ranges from sea level at the Pacific Ocean to over 1100 m at the crest of the Santa Ynez Mountains. Natural vegetation cover on the southern slope of the Santa Ynez Mountains consists of sclerophyllous evergreen chaparral, dominated by *Ceanothus megacarpus* (big pod ceanothus), *Adenostoma fasciculatum* (chamise), and *Quercus agrifolia* (coast live oak). *Arctostaphylos glandulosa* (eastwood manzanita), *Arctostaphylos glauca* (bigberry manzanita), *Ceanothus spinosus* (greenbark ceanothus), and introduced European grasses are locally abundant. Six land cover classes were chosen for mapping using MESMA, dominated by *C. megacarpus*, *A. fasciculatum*, *Q. agrifolia*, *Arctostaphylos* spp., grassland, and soil, respectively. *C. spinosus* was determined to dominate primarily at a scale less than 20 m and was not mapped. The two species of *Arctostaphylos* dominant in the Santa Ynez Mountains are often intermixed but seldom solely dominant at a resolution of 20 m, so these species were combined into a single land cover type. Grassland and soil are of particular interest for fire hazard, since the two land cover types are difficult to separate using broad band sensors and have very different implications for fire behavior.

3.2. AVIRIS data

AVIRIS is a 224-band imaging spectrometer that covers a spectral range from 400–2500 nm (Green et al., 1998). Flown at an altitude of 20 km, AVIRIS has an image swath approximately 11 km wide and an instantaneous field-of-view of approximately 20 m. Three AVIRIS scenes (614 by 512 pixels) were acquired over the Santa Barbara and the Santa Ynez Mountains on June 14, 2001. The scenes were acquired at approximately solar noon with a solar zenith of 12°. The AVIRIS scenes were processed to apparent surface reflectance using a modified version of the MODTRAN radiative transfer model (Green, Conel, & Roberts, 1993). Calculated image reflectance was calibrated using the field-measured reflectance of a large sand target. AVIRIS reflectance data were registered to an orthorectified SPOT mosaic projected to Universal Transverse Mercator (UTM; zone 11; North American Datum 1983) and resampled to a resolution 20 m.

3.3. Reference data

Reference polygons used for the endmember selection and accuracy assessment were mapped using field-assessed vegetation cover and orthophotographs. Each reference polygon was determined to meet the following requirements:

1. Size greater than 40 by 40 m, so that at least one 20-m AVIRIS pixel fell entirely within the polygon.

2. Dominated by a single land cover type (vegetation species, grassland, or soil) that was at least 50% dominant.
3. Uniform slope and aspect at the pixel scale.

A total of 74 reference polygons were identified in the field in June 2002. Six classes were used to facilitate rapid identification of land cover dominance in the field. Land cover dominance was categorized based on percent cover into one of six classes: 0–10%, 10–25%, 25–50%, 50–75%, 75–90%, and 90–100%. The coverage classes of the dominant land cover (based on the six land cover classes) and subdominant land covers (not limited to the six land cover classes) were described for the top three constituents of each polygon. Polygons were mapped on hardcopy United States Geological Survey (USGS) 1-m resolution grayscale digital orthophoto quads (DOQs).

3.4. Spectral library

A spectral library was constructed from image spectra extracted from the registered AVIRIS scenes. Reference polygons were digitized and image spectra were extracted from 57 polygons that were 75–90% or 90–100% dominated by a single land cover class. Image spectra were not extracted from the 50–75% dominated polygons due to concerns about decreased spectral purity with decreased dominance. AVIRIS image pixels entirely inside reference polygons were included in the spectral library. Pixels only partially inside polygons were excluded to avoid spectral mixing of the dominant land cover type with other land cover types outside the reference polygon. A total of 915 spectra were included in the spectral library (Table 1).

The library of 915 image spectra was unmixed by each component spectrum and shade using MESMA, so that a total of 914 unique two endmember models were run for each spectrum. Models were fit using modified Gram–Schmidt orthogonalization (Golub & Van Loan, 1989). The best-fit linear models were subject to constraints empirically determined to be optimal by Halligan (2002). Halligan found that the accuracy of hyperspectral land cover mapping in Yellowstone National Park using MESMA using MESMA was highest when endmember fractions were constrained to 106%. For this paper, land cover endmember fractions were constrained to less than 106%.

Table 1
Number of representative spectra in each land cover class

Land cover class	Spectra
<i>C. megacarpus</i>	398
Grassland	129
<i>Q. agrifolia</i>	125
<i>Arctostaphylos</i> spp.	111
<i>A. fasciculatum</i>	76
Soil	76
Total	915

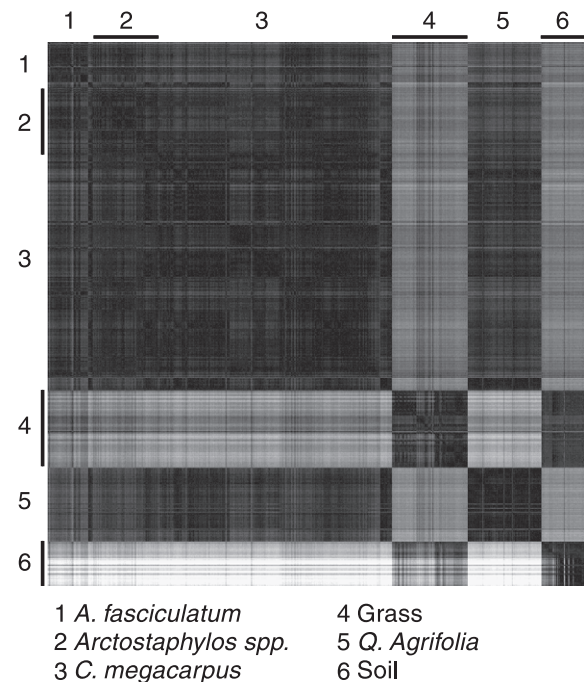


Fig. 1. An image of RMSE resulting from unmixing the spectral library against itself. Endmember spectra are on the x-axis and modeled spectra are on the y-axis. Classes are ordered by number. The bright bands are higher RMSE values resulting from grass and soil modeling green vegetation. Zero values mark the diagonal where a spectrum models itself.

For best-fit models with land cover endmember fractions above 106% RMSE was calculated using an endmember fraction of 106%. No constraints were placed on model residuals or RMSE to allow the creation of a complete RMSE matrix (Fig. 1). The brightness of each cell in the matrix indicates the RMSE for the endmember on the x-axis modeling the spectrum on the y-axis. The RMSE matrix is not symmetrical due to the brightness constraint placed on the mixing models. An endmember modeling a spectrum more than 106% brighter than itself possesses a high RMSE because the maximum non-shade fraction is constrained to 106%.

3.5. Class average RMSE (CAR)

CAR was used to determine potential confusion between land cover classes. CAR was calculated as the average RMSE for one land cover class unmixing another. If endmembers from class *A* are modeling spectra from class *B*,

$$CAR_{A,B} = \frac{\sum_{i=1}^m \sum_{j=1}^n RMSE_{A_i,B_j}}{m*n} \quad (4)$$

where *m* is equal to the number of endmembers in class *A* and *n* is equal to the number of modeled spectra in class *B*. In the special case of a class modeling itself, *m* is equal to

n and the class diagonal will be modeled with zero RMSE. The number of unique, non-zero models then becomes $n^2 - n$, so that

$$CAR_{A,A} = \frac{\sum_{i=1, j=1}^n RMSE_{A_i, A_j}}{n^2 - n} \quad (5)$$

CAR is equivalent to averaging the RMSE for all the models within a square defined by two land cover classes on the model image (Fig. 2). Land cover classes used for each CAR can be the average of a single class modeling itself (*C. megacarpus* unmixing *C. megacarpus*) or the average of a class modeling a different class (*Q. agrifolia* unmixing *C. megacarpus*). In Fig. 2, an example of CAR is shown as the average RMSE of all models where *Q. agrifolia* spectra unmix *C. megacarpus* spectra.

CAR was used to evaluate the likelihood of confusion between land cover classes. CAR calculated for each combination of classes produces a confusion matrix that permits a relative assessment of modeling error. If the average RMSE of one class unmixing another class is lower or similar to the average RMSE of that class unmixing itself, then confusion between those two classes is probable. For example, *C. megacarpus* endmembers may unmix *Q. agrifolia* image spectra better (with lower class average RMSE) than *Q. agrifolia* endmembers themselves. CAR is also an indicator of within-class spectral variability. For example, both senesced grass and green grass spectra could be included in a grassland

land cover type. Senesced grass endmembers will model green grass spectra poorly and green grass endmembers will model senesced grass spectra poorly. Within-class CAR will be lowest for the spectrally most homogeneous classes.

3.6. Endmember average RMSE (EAR)

EAR was used to select a representative endmember for each land cover class. EAR was calculated for each endmember by averaging the RMSE of the set of models that use that endmember to unmix the spectra belonging to the same land cover class:

$$EAR_{A_i, A} = \frac{\sum_{j=1}^n RMSE_{A_i, A_j}}{n - 1} \quad (6)$$

where A is the endmember class, A_i is the modeled spectra class, n is the number of spectra in class A , and A_j is the endmember. The term $n - 1$ accounts for the endmember modeling itself, which produces a zero RMSE. EAR is equivalent to averaging the RMSE for all the models of a single endmember within the same land cover class (Fig. 2). The modeled spectra within the *C. megacarpus* land cover class included in the EAR for spectrum 2 are highlighted in light gray. The EAR for spectrum 2 is the average of the model RMSE for endmember 2 unmixing all the spectra within the *C. megacarpus* class. In the actual spectral library, the EAR for a single *C. megacarpus* endmember was calculated as the average RMSE for the 397 *C. megacarpus* spectra it modeled.

EAR was used to evaluate the ability of each endmember to model the spectra within its own class. EAR does not provide a measure of endmember “purity”, but rather measures the actual performance of an endmember for unmixing spectra within its own class. The endmember with the minimum EAR was selected to map the AVIRIS scene. Endmembers possessing a lower EAR model spectra within their land cover class better than endmembers with a higher EAR. The minimum EAR endmember should be the most representative of its modeled class. Again, the spectral diversity within a class plays a role. If the spectra within a class are very diverse and possess a high CAR, the endmember with the lowest EAR may be representative of only a portion of the class, or in the worst case not representative of the class at all.

3.7. Endmember models

Endmembers selected by EAR were used with MESMA to map class and class fraction in the AVIRIS image. A hierarchical approach that allows for both two and three endmember models was used. The image was modeled using 6 two endmember models (using the minimum EAR

		Endmember Spectra													
		<i>C. megacarpus</i>					<i>Q. agrifolia</i>								
		1	2	3	4	5	1	2	3	4					
Modeled Spectra	<i>C. megacarpus</i>	1													
	2														
	3		E									A			
	4		A									R			
	5		R												
	<i>Q. agrifolia</i>	1													
2															
3															
4															

Fig. 2. A diagrammatic example of endmember average RMSE (EAR; light gray) and class average RMSE (CAR; dark gray). The spectral library in this example has nine spectra, with five *C. megacarpus* spectra and four *Q. agrifolia* spectra. Endmembers that model themselves along the diagonal are not included in CAR or EAR.

endmember for each class and shade) and 9 three endmember models. For the three endmember case, the minimum EAR endmember was used to create the following models:

1. The four minimum EAR green vegetation endmembers (*A. fasciculatum*, *Arctostaphylos* spp., *C. megacarpus*, and *Q. agrifolia*), the minimum EAR grassland endmember and photometric shade (four total).
2. The minimum EAR green vegetation endmembers, the minimum EAR soil endmember, and shade (four total).
3. The minimum EAR grassland endmember, the minimum EAR soil endmember, and shade.

Fraction constraints for both the two endmember and the three endmember models were set to be equivalent to the constraints used for creating the model image. Non-shade fractions were constrained to between -6% and 106% . Additional constraints were also placed on the models. Residuals were not allowed to exceed 2.5% reflectance for more than seven contiguous bands (Roberts et al., 1998), and RMSE was constrained to below 2.5% reflectance.

For each pixel, the lowest RMSE two endmember model and the lowest RMSE three endmember model were selected and compared. The three endmember model was assigned to the pixel if the two endmember model did not meet the model constraints. If neither model met the constraints, then the pixel was left as unmodeled. If both the minimum RMSE two and three endmember models fit the pixel spectrum, the two models were compared. Three endmember models will always have lower RMSE than two endmember models, but the improvement may not significantly change endmember fractions. Simpler two endmember models are preferred over more complex three endmember models, except in cases where adding an endmember significantly improves RMSE. Using the same AVIRIS scene, Roberts et al. (in press) empirically determined that an RMSE improvement of 0.8% reflectance justified selection of the three endmember model. In this study, three endmember models were selected over two endmember models where the three endmember model improved RMSE by more than 0.8% reflectance.

4. Results

4.1. CAR

Table 2 shows the matrix of CAR values calculated for all combinations of land cover classes. Columns show CAR for each endmember class, while rows show CAR for each modeled spectrum class. Within-class CAR is found along the diagonal. Within-class CAR is a measure of the spectral variability within a land cover class. A high within-class CAR indicates endmembers may poorly model the spectra within their own class. Soil has the highest within-class CAR, a product of the high spectral variability of soils and variable subdominant vegetation fraction. *A. fasciculatum* also has a high within-class CAR, and *A. fasciculatum* endmembers unmixed *Arctostaphylos* spp. spectra slightly better than they unmixed the spectra within their own class. Variable soil fraction at sub-pixel resolution could contribute to both the higher within-class spectral variability of the *A. fasciculatum* class and the low CAR of *A. fasciculatum* unmixed *Arctostaphylos* spp. Grassland also demonstrated a high within-class CAR, which can be attributed to variable expression of grassland senescence and soil in the spectra of this class.

Between-class CAR is a measure of the spectral confusion between land cover classes. Grassland and soil are very distinct from the green vegetation land cover classes (high between-class CAR), while the between-class CAR between green vegetation classes was generally much lower (Table 2). *Arctostaphylos* spp., *C. megacarpus*, and *Q. agrifolia* endmembers modeled spectra within their class better on average than they modeled spectra in other classes. Modeled classes with between-class CAR values less than 2.5% , the RMSE threshold used for MESMA class mapping, may highlight possible confusion between classes in the final map. *A. fasciculatum* was best modeled by itself, but was also modeled by *Arctostaphylos* spp. *Arctostaphylos* spp. was modeled by itself, *C. megacarpus*, and *A. fasciculatum*. *Arctostaphylos* and *Q. agrifolia* modeled *C. megacarpus* below a CAR threshold of 2.5% , while *Q. agrifolia*, grassland, and soil were only modeled by themselves below this threshold. Based on this analysis, these three land cover classes are more distinct and less likely to be modeled by

Table 2
Class average RMSE (CAR) for the six land cover classes, in percent reflectance

Modeled class	Endmember class					
	<i>A. fasciculatum</i>	<i>Arctostaphylos</i> spp.	<i>C. megacarpus</i>	Grassland	<i>Q. agrifolia</i>	Soil
<i>A. fasciculatum</i>	2.26%	2.49%	3.11%	7.35%	4.58%	8.24%
<i>Arctostaphylos</i> spp.	2.20%	1.45%	2.08%	8.17%	3.34%	8.92%
<i>C. megacarpus</i>	2.54%	1.90%	1.63%	8.60%	2.39%	9.42%
Grassland	9.36%	10.88%	11.73%	2.53%	13.67%	2.92%
<i>Q. agrifolia</i>	4.52%	3.58%	2.87%	11.10%	1.38%	11.94%
Soil	18.43%	20.07%	21.12%	10.61%	22.51%	3.57%

The endmember classes are listed in the first row and the modeled spectra classes are listed in the first column. Values are percent reflectance.

Table 3
Spectra from each land cover class with the lowest endmember average RMSE

Class	Endmember	EAR	Bright	Green	Z _{bright}	Z _{green}
<i>A. fasciculatum</i>	adfa030	1.61%	0.35	0.15	0.20	0.11
<i>Arctostaphylos</i> spp.	argl022	1.08%	0.33	0.15	-0.36	-0.06
<i>C. megacarpus</i>	ceme247	1.08%	0.32	0.18	0.79	0.25
Grassland	gras104	1.42%	0.49	0.03	1.50	-0.31
<i>Q. agrifolia</i>	quag119	0.89%	0.31	0.24	0.66	0.66
Soil	soil026	1.27%	0.73	0.00	0.90	-0.41

EAR values are percent reflectance. Also shown are brightness (bright) and greenness (green) values from a tasseled cap transformation, and the z-scores for these brightness and greenness values within each land cover class.

endmembers from other land cover classes. Based on CAR, confusion between land cover classes is most likely to occur for the three chaparral classes: *A. fasciculatum*, *Arctostaphylos* spp., and *C. megacarpus*.

4.2. EAR

EAR was calculated for a total of 915 spectra within 6 land cover classes. The endmember with the minimum EAR was selected from each land cover class (Table 3). *Q.*

agrifolia had the lowest EAR value among the six land cover classes. *A. fasciculatum*, grassland, and soil endmembers had higher minimum EAR values, demonstrating the higher within-class spectral variability of these land cover classes. To assess the extremeness of the selected endmembers, a tasseled cap transformation (Crist, 1985; Kauth & Thomas, 1976) was used to measure the relative brightness and greenness of each endmember in comparison its class. AVIRIS reflectance data were convolved to Landsat TM and brightness and greenness were calculated using the coefficients from Crist (1985). To facilitate comparison between land cover classes, brightness and greenness were standardized using the mean and standard deviation of each land cover class. The z-score was calculated as

$$z = \frac{x - \mu}{\sigma_x} \tag{7}$$

where *x* is the brightness or greenness value of the selected endmember, μ is the mean brightness or greenness of the land cover class, and σ_x is the standard deviation of the selected endmember. The brightness, greenness, and z-scores of each minimum EAR endmember are displayed in Table 3.

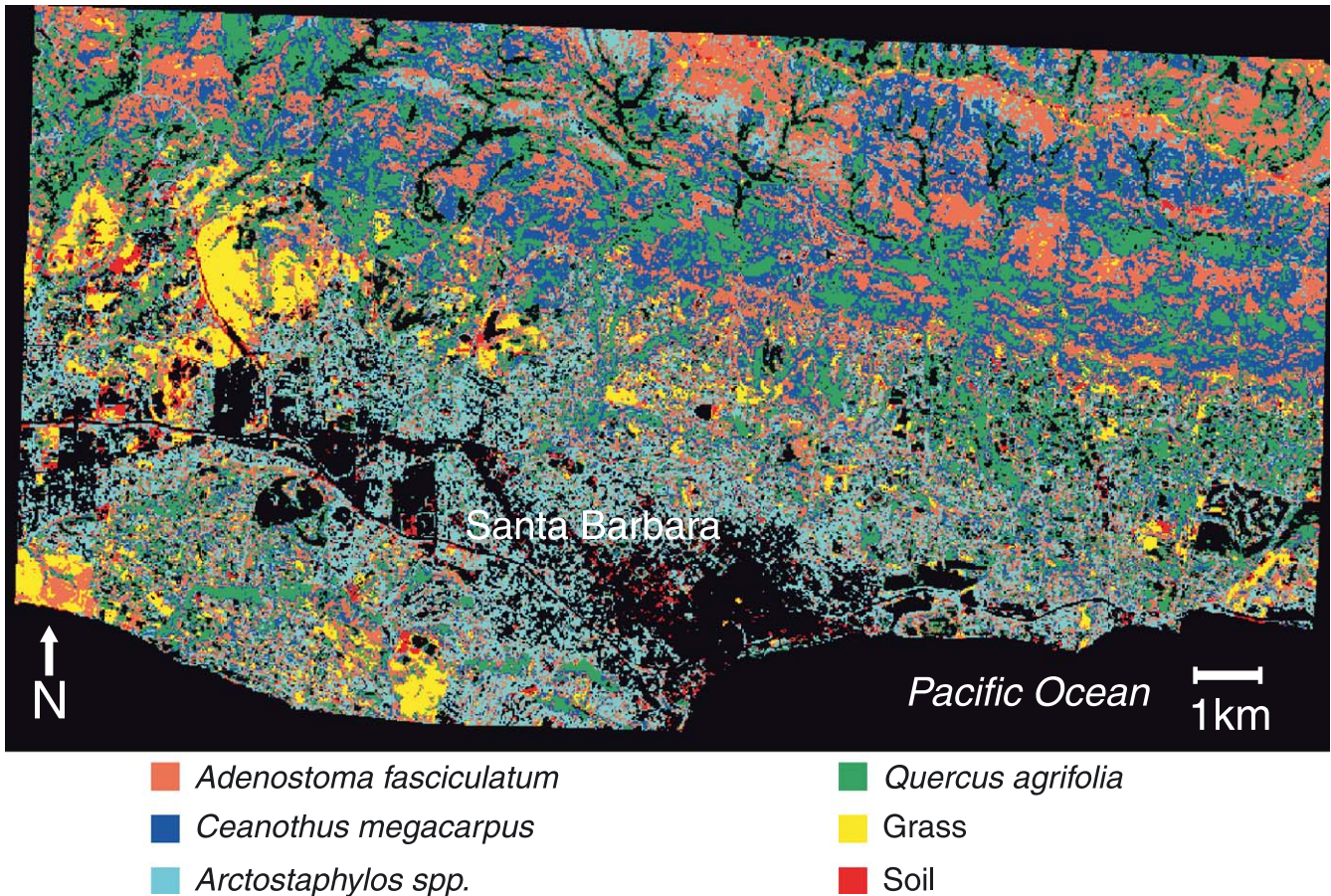


Fig. 3. Dominant land cover class mapped by the minimum EAR endmembers using MESMA. Black areas are unmodeled. From south to north, the major features in the image are the Pacific Ocean, urban Santa Barbara, and the Santa Ynez Mountains.

Transformed greenness and brightness demonstrate discernable trends in the minimum EAR endmembers selected for each land cover class (Table 3). All of the minimum EAR endmembers, with the exception of *Arctostaphylos*, possessed higher-than-average brightness ($Z > 0$). Green vegetation endmembers had slightly higher than average greenness, while grassland and soil endmembers had slightly lower than average greenness. Brightness and greenness values for nearly all of the selected endmembers were not found to be extreme. All greenness values and all but one brightness value were within one standard deviation of the mean of the land cover class. The grassland minimum EAR endmember was the most extreme in brightness, with a Z-score of 1.5. The wide range in the spectral brightness of grasslands, dependent on the height of the grass and the degree of senescence, likely favored the selection of a brighter endmember that could model both brighter and darker grass.

4.3. Mapping

The selected minimum EAR endmembers were used to model the AVIRIS image. A dominant land cover class map resulting from the minimum RMSE derived from two and from three endmember models is shown in Fig. 3. The Pacific Ocean is evident along the lower edge of the image,

and the mostly unmodeled area in the lower half of the image is urban Santa Barbara. The south facing slope of the Santa Ynez Mountains comprises the top half of the image. Twenty-four percent of the image was not modeled, largely due to the absence of urban and ocean spectral classes. Urban vegetation was frequently modeled as the *Arctostaphylos* spp. land cover class. The endmembers from this class contain green vegetation, rock, and non-photosynthetic vegetation spectral components, making them the best model for the highly heterogeneous urban landscapes.

If urban and ocean areas are excluded, the percentage of the image modeled by the selected endmembers climbs considerably to 93.1%. Urban areas were masked using the 1998 urban extent of Santa Barbara resampled to 20 m resolution. The 59.3% of the masked image was modeled by two endmember models and 33.8% of the masked image was modeled by three endmember models. The 27.0% of the masked image was mapped as *C. megacarpus*, 26.9% as *A. fasciculatum*, 26.2% as *Q. agrifolia*, 6.3% as *Arctostaphylos* spp., 5.4% as grassland, and 1.2% as soil. Qualitatively, the map (Fig. 3) is a good approximation of the distribution of these land cover types. *C. megacarpus* is dominant on the lower slopes, while *A. fasciculatum* and *Arctostaphylos* occur most frequently at higher elevations. *Q. agrifolia* is correctly placed in canyons and on north facing slopes and grasslands are largely confined to the

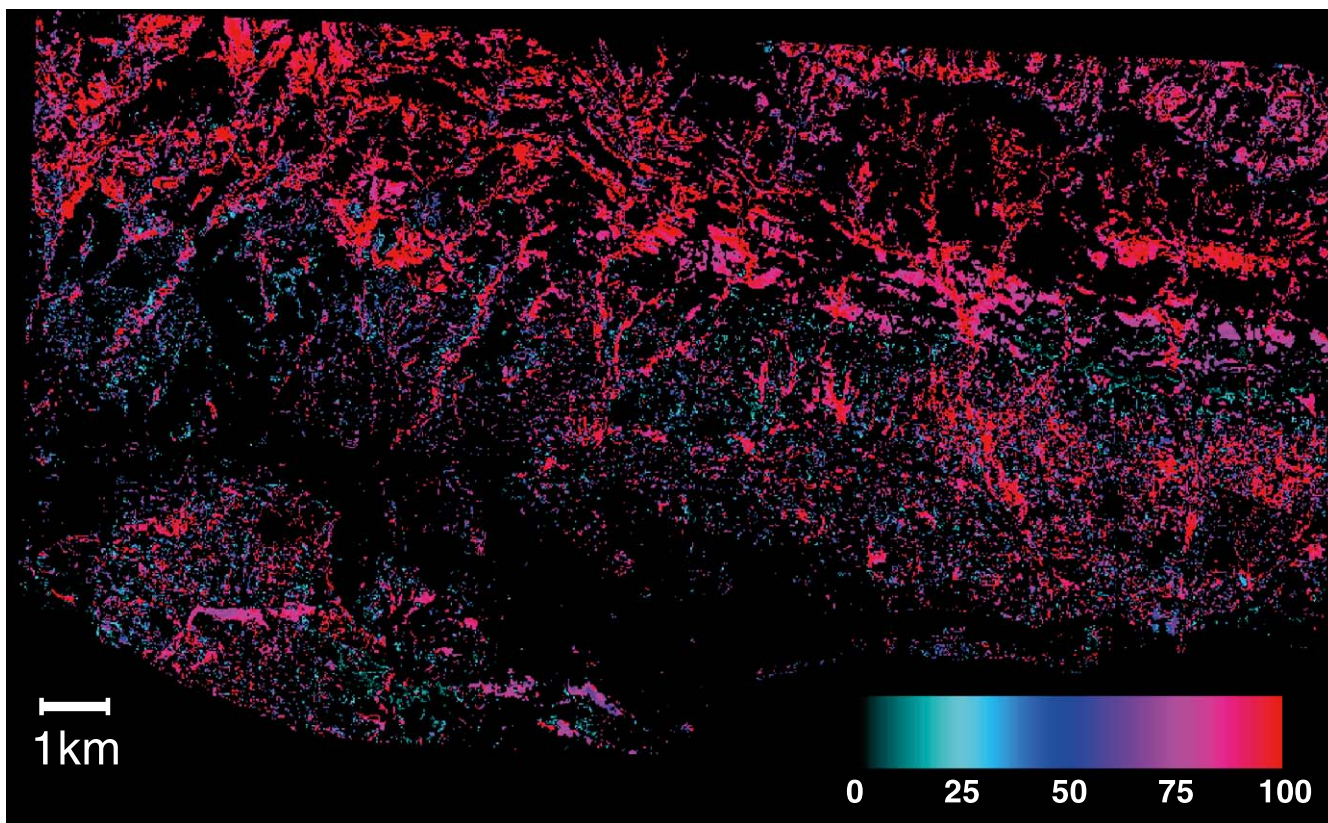


Fig. 4. A fraction image of the *Q. agrifolia* land cover class.

foothills of the Santa Ynez Mountains. The unmodeled areas, comprising 6.9% of the masked image, are predominantly riparian vegetation. These areas are dominated by *Q. agrifolia*, *Umbellularia californica* (california bay laurel), and *Platanus racemosa* (western sycamore). The inability of the selected *Q. agrifolia* endmembers to model these areas is discussed in the next section.

Fraction images were constructed using the modeled fraction from the selected two or three endmember model. The modeled fractions for *Q. agrifolia* and grassland land cover classes are shown as examples of fraction images (Figs. 4 and 5). The modeled fractions displayed in these figures have not been normalized by their corresponding shade fraction. Shade normalization divides each non-shade fraction by the sum of all non-shade fractions, and in two endmember models produces uniform normalized fractions of 100%. In the *Q. agrifolia* fraction image (Fig. 4), fractions are highest in the canyons and north facing slopes immediately north of Santa Barbara. Less contiguous and lower *Q. agrifolia* fractions are also found in the wildland urban interface, where this class is likely mapping both *Q. agrifolia* in residential areas as well as ornamental trees. The grassland fraction image (Fig. 5) highlights several areas with high grassland fraction, including parks in Santa Barbara (lower left) and pasture (middle left). Brightness is likely a large control on grassland fraction, since the areas with the highest fractions in this image are largely short

grass pastures. Taller ungrazed grass possesses lower grassland fraction, as shadows cast by the stems increases the shade fraction.

5. Accuracy

The accuracy of the modeled dominant land cover class and fractions for each polygon was assessed using the entire set of reference polygons. All 74 reference polygons, each at least 50% dominated by a single land cover class, were used. Since the reference polygons were selected using a purity constraint, accuracy assessed using the polygons may not reflect the accuracy of more heterogeneous areas within the modeled image. Modeled class and fractional coverage for pixels entirely within each reference polygon were extracted from the image. Land cover class accuracy was assessed by grouping all the pixels within a polygon and selecting the most frequently modeled dominant land cover class as the dominant class for the polygon. User's accuracies, representing errors of commission, and producer's accuracies, representing errors of omission, were calculated for each land cover class. Four polygons were excluded from the land cover class accuracy assessment because of ties between dominant classes. Fraction accuracy was assessed by normalizing the fractions and calculating the mean fractions of all land cover classes for all the pixels

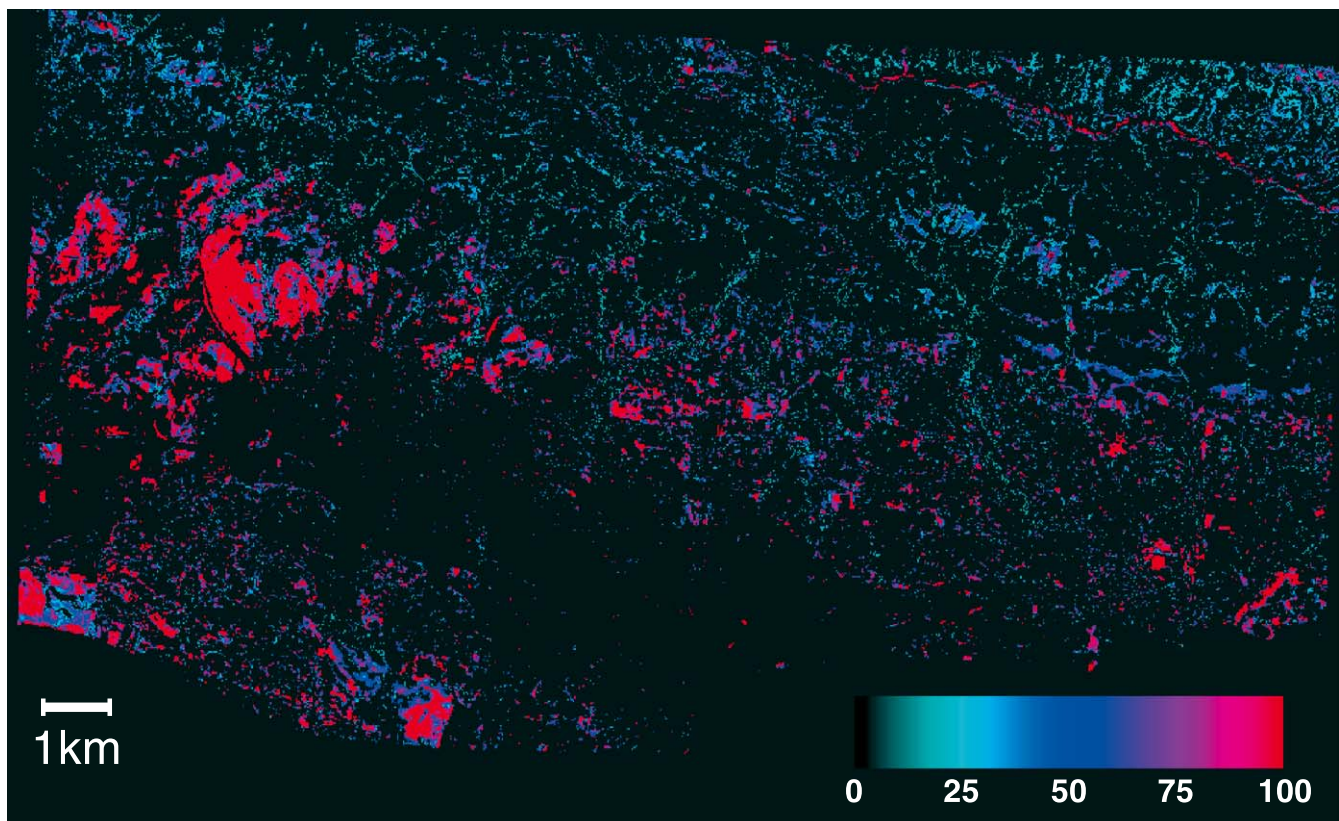


Fig. 5. A fraction image of the grassland cover class.

Table 4
Polygon dominant land cover class confusion matrix, including user's and producer's accuracies

Image dominant	Reference dominant							User's
	<i>A. fasciculatum</i>	<i>Arctostaphylos</i> spp.	<i>C. megacarpus</i>	Grass	<i>Q. agrifolia</i>	Soil	Unmodeled	
<i>A. fasciculatum</i>	13	0	1	0	0	0	0	0.93
<i>Arctostaphylos</i> spp.	0	4	0	0	0	0	0	1.00
<i>C. megacarpus</i>	0	2	19	0	0	0	0	0.90
Grass	0	0	0	12	0	0	0	1.00
<i>Q. agrifolia</i>	0	0	4	0	8	0	0	0.67
Soil	0	0	0	0	0	6	0	1.00
Unmodeled	0	0	0	0	0	1	0	0.00
Producer's	1.00	0.67	0.79	1.00	1.00	0.86	–	

within a polygon. For the reference polygons, land cover classes that were not recorded as one of the top three dominant or subdominant classes were given a fraction of 0%. The mean modeled fractions were binned to match the categories used for describing dominance in the reference polygons: 0%, 0–10%, 10–25%, 25–50%, 50–75%, 75–90%, and 90–100%.

The confusion matrix comparing reference dominant land cover class and modeled dominant land cover class is displayed in Table 4. Dominance was correctly assigned for 62 of the 70 reference polygons, giving an overall accuracy of 88.6%. κ was calculated as 0.86 (Cohen, 1960; Congalton, 1991). This represents an improvement over previous efforts. Previous work mapping vegetation in the study area using MESMA produced an overall accuracy of 79.1% and a κ of 0.72 (Roberts et al., in press). User's accuracies ranged from 67% for *Q. agrifolia* to 100% for *Arctostaphylos*, grassland, and soil (Table 4). Producer's accuracies ranged from 67% for *Arctostaphylos* to 100% for *A. fasciculatum*, grassland, and *Q. agrifolia*. Two out of six *Arctostaphylos* polygons were mapped as *C. megacarpus*. *C. megacarpus* also had a lower producer's accuracy, with four *C. megacarpus* polygons mapped as *Q. agrifolia*. A single *C. megacarpus* polygon was also mapped as *A. fasciculatum*. Analysis of the CAR matrix indicated that *Q. agrifolia* endmembers modeling *C. megacarpus* spectra was a probable source of confusion between vegetation classes. While the CAR matrix indicated possible confusion between *Arctostaphylos* endmembers and the spectra of the

C. megacarpus class, the selected *Arctostaphylos* endmember was dominant only in *Arctostaphylos* polygons. One soil polygon was left unmodeled because of its unusual brightness.

The confusion matrix comparing fraction classes of the reference polygons and the binned modeled fractions is shown in Table 5. A total of 444 land cover fractions within the 74 polygons were available for accuracy assessment. Overall accuracy of the modeled fractions was 55.9% with a κ of 22.1%. User's and producer's accuracies were low for all fractional coverage classes with the exception of the 0% fraction class, demonstrating that the large number of zero fractions artificially inflated the overall accuracy. Fifty-eight of the 74 reference polygons, primarily *A. fasciculatum*, *Arctostaphylos* spp., and *C. megacarpus* dominated polygons, were modeled as having at least one land cover class fraction that was not present in the polygon according to the field assessment. However, while the modeled fraction was clearly overestimated where the actual coverage was at or near 0%, 83 of the 108 overestimated fractions were modeled below 25% fractional coverage (Table 5, shaded outlined box). Underestimation of fractional coverage was a problem for reference fractions above 50%. The land cover class actually dominating the polygon was not modeled in three cases and was undermodeled in 41 of the 74 polygons (Table 5, unshaded outlined box). *C. megacarpus* and *Arctostaphylos* spp. were the two land cover types with the most consistent undermodeling of dominant reference fractions.

Table 5
The fractional coverage confusion matrix, with the shade normalized and binned fractions of each of the six land cover classes

Modeled Polygon Fractional Coverage	Reference Polygon Fractional Coverage							user's
	0%	0%-10%	10%-25%	25%-50%	50%-75%	75%-90%	90%-100%	
0%	228	4	8	2	1	0	2	0.93
0%-10%	59	2	2	1	0	0	0	0.03
10%-25%	24	4	2	2	1	0	1	0.06
25%-50%	19	1	5	1	3	4	1	0.03
50%-75%	4	0	0	0	5	13	9	0.16
75%-90%	2	0	0	0	2	1	8	0.08
90%-100%	0	0	0	0	4	10	9	0.39
producer's	0.68	0.18	0.12	0.17	0.31	0.04	0.30	

Fractions describing land cover classes that were absent from the reference data were classed as 0% fractional coverage. Modeled fractions overestimated for 0% reference fractional coverage are outlined and shaded gray. Dominant reference fractions that were underestimated are outlined and unshaded.

Pixel level spectral confusion resulting in misclassification had the greatest impact on fractional accuracy. CAR values for the three chaparral land cover classes indicated probable confusion between these classes. In most of the vegetated polygons, a minority of pixels were modeled as *A. fasciculatum*, *Arctostaphylos* spp., *C. megacarpus*, or *Q. agrifolia*. Averaging at the polygon level, the misclassification of these pixels resulted in low modeled fractions of these species being included in the polygons. For example, 18.1% of *C. megacarpus* pixels were incorrectly modeled as *Q. agrifolia*, and 27.3% of *Arctostaphylos* spp. pixels were incorrectly modeled as *A. fasciculatum*. The misclassification of pixels within the vegetation polygons also resulted in a reduction of the modeled fraction of the dominant vegetation class. As a result, dominant fractions were undermodeled in many cases (Table 5). Aggregating the modeled fractions to the polygon level decreased the fractional coverage of the misclassified pixels to below 50% in most cases, resulting in a correct classification. This fractional component was still apparent in the fractional accuracy assessment as seen in overmodeling of absent land cover classes and undermodeling of dominant land cover classes.

6. Discussion

EAR provides a method for assessing which endmembers will perform the best for mapping a hyperspectral image using MESMA. The selected minimum EAR endmembers were chosen because they best modeled the image spectra extracted from a subset of the reference polygons. These endmembers modeled the AVIRIS image and produced a land cover map of acceptable accuracy as assessed from the entire set of reference polygons. The advantage of selecting endmembers using EAR is that, unlike previous methods of selecting endmembers for MESMA, the selection is based on a measure of error central to the MESMA model. The selected endmembers are not the most pure or the most extreme, but are the most representative of their class. While EAR is demonstrated here using image endmembers, it is not limited to image spectra. EAR can also be calculated for reference or field spectra modeling themselves, or for reference or field spectra modeling image spectra.

EAR has three potential shortcomings. Endmembers with low average RMSE for modeling their own class may also have a low average RMSE for modeling another class. Since EAR is based only on the RMSE within a class, EAR does not account for spectral confusion between classes. The minimum EAR endmember from one class could potentially model another class better than that class's selected endmember. Second, EAR as it is currently presented is only applicable to two endmember models. To be more useful for land cover mapping, EAR should also be valid for three and four endmember models. Finally, EAR also does not select spectrally extreme endmembers. Extreme endmembers are not excluded from being chosen as the lowest EAR end-

members, since RMSE, which is most dependent on spectral shape, is the criterion upon which selection is based. However, extreme endmembers are not favored for selection, leaving the potential for brighter pixels in the image to remain unmodeled.

Extremeness effects were apparent in the modeled AVIRIS image. A soil polygon was classified as unmodeled because the spectra of a majority of the pixels within the polygon were too bright to be modeled by the selected minimum EAR endmember. Approximately 3% of the polygon spectra were unmodeled, most commonly in the soil and *A. fasciculatum* classes. Riparian areas in the image were not modeled, even though many of these areas are dominated by *Q. agrifolia*. The *Q. agrifolia* class did not contain endmembers that were bright or green enough to adequately model the riparian areas. In this instance, including riparian polygons, whether as part of the *Q. agrifolia* class or as their own class, likely would have improved the percentage of the image modeled.

There are several possible methods for improving EAR-based endmember selection for MESMA. CAR and EAR could be used to improve endmember selection by minimizing confusion between endmember classes. Classes likely to be confused with each other would be determined using the CAR matrix (Table 2). To reduce the apparent confusion between *Q. agrifolia* and *C. megacarpus*, for example, endmember selection could be guided by both a within-class EAR and a between-class EAR. A low average RMSE is desirable for modeling spectra within the same class, while a higher average RMSE is desirable for modeling spectra from a confused class. Selecting endmembers that model their own class well and the confused class poorly could help reduce confusion between classes. If a single EAR selected endmember is inadequate for modeling a spectrally diverse class, the methods presented here could be diversified to allow for the selection of multiple endmembers for a class. Spectra poorly modeled by the minimum EAR endmember could be subset and then modeled again. Subsequent endmembers could be chosen until the percentage of unmodeled spectra drops below a predetermined threshold. To select more extreme endmembers, endmembers could be weighted by their brightness. The most desirable endmembers would be selected based on a combination of the lowest EAR and the highest brightness. Alternatively, the endmembers in a class could be subset by their extremeness. A brighter subset could be used to model the entire class, and the minimum EAR endmembers from the subset would be selected. Other criteria, such as number of modeled pixels in the image, could also be used to guide endmember selection.

7. Conclusions

MESMA is a powerful technique for mapping the materials present in an image and their fractional coverage.

Two new measures are presented for selecting endmembers for MESMA. CAR calculates the average RMSE for same-class models (i.e. *C. megacarpus* modeling *C. megacarpus*) and for endmembers of one class modeling another class (i.e. *Q. agrifolia* modeling *C. megacarpus*). CAR highlights potential confusion between classes and spectral diversity within classes. EAR calculates the average RMSE for a single endmember modeling the spectra within its land cover class (i.e. endmember *ceme241* modeling *C. megacarpus* spectra). EAR is dependent on how well the endmember models the spectra within its land cover class. The minimum EAR endmember within a class best represents that class, and can be selected for mapping that class using MESMA.

CAR values for three chaparral land cover classes indicated the classes were spectrally similar and prone to confusion. This confusion was responsible for a consistent undermodeling of dominant land cover classes and overmodeling of absent land cover classes. Spectral confusion may be an obstacle to pixel scale mapping of chaparral species. Aggregating MESMA classification to the polygon level reduced the confusion between land cover classes, and may be necessary to produce accurate maps of vegetation cover in chaparral. Endmembers selected using EAR were able to map land cover class at the polygon level with an accuracy of 88.6%.

Future efforts will focus on expanding the capabilities of endmember selection using EAR. While developed using AVIRIS data, these endmember selection techniques can also be applied to other hyperspectral data (e.g. Hyperion) and multispectral data (e.g. Landsat TM). Hierarchical selection, measures of spectral extremeness and separability, and maximal covering may be used to select second and third endmembers for each land cover class, increasing the number and area of materials modeled. Measures of spectral separability may also be used to help determine separable land cover classes in cases where spectral confusion is probable, such as urban environments (Small, 2001). Endmember selection techniques proven in Southern California chaparral will be applied to vegetated ecosystems for mapping of species, arid ecosystems for mapping of vegetation and soil types, and urban environments for mapping of urban materials.

Acknowledgements

Support for this research was provided by a National Aeronautics and Space Administration (NASA) Earth Systems Science Fellowship (NGT5-50327), and the NASA Solid Earth and Natural Hazards (NAG2-1140), Regional Earth Science Application Center (CSDH NASA RESAC 447633-59075), and EO-1 Science Validation (NCC5-496) programs. We also wish to thank the Jet Propulsion Laboratory for providing radiometrically calibrated AVIRIS data and the reviewers for their helpful comments.

References

- Adams, J. B., Smith, M. O., & Gillespie, A. R. (1993). Imaging spectroscopy: Interpretation based on spectral mixture analysis. In C. M. Pieters, P. A. J. Englert (Eds.), *Remote geochemical analysis: Elemental and mineralogical composition* (pp. 145–166). Cambridge, England: Press Syndicate of Univ. of Cambridge.
- Adams, J. B., Smith, M. O., & Johnson, P. E. (1986). Spectral mixture modeling: A new analysis of rock and soil types at the Viking Lander I site. *Journal of Geophysical Research*, *91*, 8098–8812.
- Asner, G. P., Bateson, C. A., Privette, J. L., Elsaleous, N., & Wessman, C. A. (1998). Estimating vegetation structural effects on carbon uptake using satellite data fusion and inverse modeling. *Journal of Geophysical Research—Atmospheres*, *103*, 28839–28853.
- Bateson, A., & Curtiss, B. (1996). A method for manual endmember selection and spectral unmixing. *Remote Sensing of Environment*, *55*, 229–243.
- Bateson, C. A., Asner, G. P., & Wessman, C. A. (2000). Endmember bundles: A new approach to incorporating endmember variability into spectral mixture analysis. *IEEE Transactions on Geoscience and Remote Sensing*, *38*, 1083–1094.
- Bell, J. F., Farrand, W. H., Johnson, J. R., & Morris, R. V. (2002). Low abundance materials at the Mars Pathfinder landing site: An investigation using spectral mixture analysis and related techniques. *Icarus*, *158*, 56–71.
- Boardman, J. W. (1993). Automating spectral unmixing of AVIRIS data using convex geometry concepts. *Summaries of the Fourth Annual JPL Airborne Geoscience Workshop* (pp. 11–14). Pasadena, CA: Jet Propulsion Laboratory.
- Boardman, J. W., Kruse, F. A., & Green, R. O. (1995). Mapping target signatures via partial unmixing of AVIRIS data. *Summaries of the Fifth Annual JPL Airborne Geoscience Workshop* (pp. 23–26). Pasadena, CA: Jet Propulsion Laboratory.
- Borel, C. C., & Gerstl, S. A. W. (1994). Nonlinear spectral mixing models for vegetative and soil surfaces. *Remote Sensing of Environment*, *47*, 403–416.
- Church, R., & Reville, C. (1974). The maximal covering location problem. *Papers of the Regional Science Association*, *32*, 101–118.
- Cohen, J. (1960). A coefficient of agreement for nominal scales. *Educational and Psychological Measurement*, *20*, 37–46.
- Congalton, R. (1991). A review of assessment the accuracy of classifications of remotely sensed data. *Remote Sensing of Environment*, *37*, 35–46.
- Crist, E. P. (1985). A TM tasseled cap equivalent transformation for reflectance factor data. *Remote Sensing of Environment*, *17*, 301–306.
- Cross, A. M., Settle, J. J., Drake, N. A., & Paivinen, R. T. M. (1991). Subpixel measurement of tropical forest cover using AVHRR data. *International Journal of Remote Sensing*, *12*, 1119–1129.
- Dennison, P. E., Roberts, D. A., & Regelbrugge, J. (2000). Characterizing chaparral fuels using combined hyperspectral and synthetic aperture radar. *Proceedings of the Ninth JPL Airborne Earth Science Workshop* (pp. 119–124). Pasadena, CA: Jet Propulsion Laboratory.
- Elmore, A. J., Mustard, J. F., Manning, S. J., & Lobell, D. B. (2000). Quantifying vegetation change in semiarid environments: Precision and accuracy of spectral mixture analysis and the normalized difference vegetation index. *Remote Sensing of Environment*, *73*, 87–102.
- Garcia, M., & Ustin, S. L. (2001). Detection of interannual vegetation responses to climatic variability using AVIRIS data in a coastal savanna in California. *IEEE Transactions on Geoscience and Remote Sensing*, *39*, 1480–1490.
- Gillespie, A. R., Smith, M. O., Adams, J. B., Willis, S. C., Fischer, A. F., & Sabol, D. E. (1990). Interpretation of residual images: spectral mixture analysis of AVIRIS images, Owens Valley, California. *Proceedings of the Second Airborne Imaging Spectrometer Data Analysis Conference* (pp. 243–270). Pasadena, CA: Jet Propulsion Laboratory.
- Golub, G. H., & Van Loan, C. F. (1989). *Matrix computations*. Baltimore, MD: Johns Hopkins Univ. Press.

- Green, R., Conel, J., & Roberts, D. (1993). Estimation of aerosol optical depth and additional atmospheric parameters for the calculation of apparent surface reflectance from radiance as measured by the Airborne Visible-Infrared Imaging Spectrometer (AVIRIS). *Summaries of the Fourth Annual JPL Airborne Geosciences Workshop* (pp. 73–76). Pasadena, CA: Jet Propulsion Laboratory.
- Green, R. O., Eastwood, M. L., Sarture, C. M., Chrien, T. G., Aronsson, M., Chippendale, B. J., Faust, J. A., Pavri, B. E., Chovit, C. J., Solis, M., Olah, M. R., & Williams, O. (1998). Imaging spectroscopy and the Airborne Visible/Infrared Imaging Spectrometer (AVIRIS). *Remote Sensing of Environment*, 65, 227–248.
- Haboudane, D., Bonn, F., Royer, A., Sommer, S., & Mehl, W. (2002). Land degradation and erosion risk mapping by fusion of spectrally-based information and digital geomorphometric attributes. *International Journal of Remote Sensing*, 23, 3795–3820.
- Hall, F. G., Shimabukuro, Y. E., & Huemmrich, K. F. (1995). Remote sensing of forest biophysical structure using mixture decomposition and geometric reflectance models. *Ecological Applications*, 5, 993–1013.
- Halligan, K. Q. (2002). *Multiple endmember spectral mixture analysis of vegetation in the northeast corner of Yellowstone national park*. Master's Thesis, University of California Santa Barbara.
- Huete, A. R. (1986). Separation of soil–plant spectral mixtures by factor analysis. *Remote Sensing of Environment*, 19, 237–251.
- Kameyama, S., Yamagata, Y., Nakamura, F., & Kaneko, M. (2001). Development of WTI and turbidity estimation model using SMA—application to Kushiro Mire, eastern Hokkaido, Japan. *Remote Sensing of Environment*, 77, 1–9.
- Kauth, R. J., & Thomas, G. S. (1976). The tasseled cap—a graphic description of the spectral–temporal development of agricultural crops as seen by Landsat. *Proceedings of the symposium on machine processing of remotely sensed data* (pp. 4B41–4B51). West Lafayette, IN: Purdue University.
- Li, L., & Mustard, J. F. (2003). Highland contamination in lunar mare soils: Improved mapping with multiple endmember spectral mixture analysis (MESMA). *Journal of Geophysical Research—Planets*, 108 (E6), 7-1 to 7-14.
- Maselli, F. (1998). Multiclass spectral decomposition of remotely sensed scenes by selective pixel unmixing. *IEEE Transactions on Geoscience and Remote Sensing*, 36, 1809–1820.
- Metternicht, G. I., & Fermont, A. (1998). Estimating erosion surface features by linear mixture modeling. *Remote Sensing of Environment*, 64, 254–265.
- Mustard, J. F., & Head, J. W. (1996). Buried stratigraphic relationships along the southwestern shores of Oceanus Procellarum—implications for early lunar volcanism. *Journal of Geophysical Research—Planets*, 101, 18913–18925.
- Okin, G. S., Roberts, D. A., Murray, B., & Okin, W. J. (2001). Practical limits on hyperspectral vegetation discrimination in arid and semiarid environments. *Remote Sensing of Environment*, 77, 212–225.
- Painter, T. H., Dozier, J., Roberts, D. A., Davis, R. E., & Green, R. O. (2003). Retrieval of subpixel snow-covered area and grain size from imaging spectrometer data. *Remote Sensing of Environment*, 85, 64–77.
- Painter, T. H., Roberts, D. A., Green, R. O., & Dozier, J. (1998). The effect of grain size on spectral mixture analysis of snow-covered area from AVIRIS data. *Remote Sensing of Environment*, 65, 320–332.
- Peddle, D. R., Brunke, S. P., & Hall, F. G. (2001). A comparison of spectral mixture analysis and ten vegetation indices for estimating boreal forest biophysical information from airborne data. *Canadian Journal of Remote Sensing*, 27, 627–635.
- Peddle, D. R., Hall, F. G., & LeDrew, E. F. (1999). Spectral mixture analysis and geometric–optical reflectance modeling of boreal forest biophysical structure. *Remote Sensing of Environment*, 67, 288–297.
- Phinn, S., Stanford, M., Scarth, P., Murray, A. T., & Shyy, P. T. (2002). Monitoring the composition of urban environments based on the vegetation–impervious surface–soil (VIS) model by subpixel analysis techniques. *International Journal of Remote Sensing*, 23, 4131–4153.
- Pinet, P. C., Shevchenko, V. V., Chevrel, S. D., Daydou, Y., & Rosemberg, C. (2000). Local and regional lunar regolith characteristics at Reiner Gamma Formation: Optical and spectroscopic properties from Clementine and Earth-based data. *Journal of Geophysical Research—Planets*, 105, 9457–9475.
- Ray, T. W., & Murray, B. C. (1996). Nonlinear spectral mixing in desert vegetation. *Remote Sensing of Environment*, 55, 59–64.
- Riano, D., Chuvieco, E., Ustin, S., Zomer, R., Dennison, P., Roberts, D., & Salas, J. (2002). Assessment of vegetation regeneration after fire through multitemporal analysis of AVIRIS images in the Santa Monica Mountains. *Remote Sensing of Environment*, 79, 60–71.
- Roberts, D. A., Dennison, P. E., Gardner, M., Hetzel, Y. L., Ustin, S. L., & Lee, C. (2003). Evaluation of the potential of Hyperion for fire danger assessment by comparison to the airborne visible infrared imaging spectrometer. *IEEE Transactions on Geoscience and Remote Sensing* (in press).
- Roberts, D. A., Dennison, P. E., Ustin, S. L., Reith, E., & Morais, M. E. (1999). Development of a regionally specific library for the Santa Monica Mountains using high resolution AVIRIS data. *Proceedings of the Eight AVIRIS Earth Science Workshop* (pp. 349–354). Pasadena, CA: Jet Propulsion Laboratory.
- Roberts, D. A., Gardner, M., Church, R., Ustin, S., Scheer, G., & Green, R. O. (1998). Mapping chaparral in the Santa Monica Mountains using multiple endmember spectral mixture models. *Remote Sensing of Environment*, 65, 267–279.
- Roberts, D. A., Gardner, M., Church, R., Ustin, S. L., & Green, R. O. (1997). Optimum strategies for mapping vegetation using multiple endmember spectral mixture models. *Imaging spectrometry III* (pp. 108–119). Bellingham, WA: SPIE Optical Engineering Press.
- Roberts, D. A., Green, R. O., & Adams, J. B. (1997). Temporal and spatial patterns in vegetation and atmospheric properties from AVIRIS. *Remote Sensing of Environment*, 62, 223–240.
- Roberts, D. A., Numata, I., Holmes, K., Batista, G., Krug, T., Monteiro, A., Powell, B., & Chadwick, O. A. (2002). Large area mapping of land-cover change in Rondonia using multitemporal spectral mixture analysis and decision tree classifiers. *Journal of Geophysical Research—Atmospheres*, 107, 8073.
- Roberts, D. A., Smith, M. O., & Adams, J. B. (1993). Green vegetation nonphotosynthetic vegetation and soils in AVIRIS data. *Remote Sensing of Environment*, 44, 255–269.
- Rogan, J., Franklin, J., & Roberts, D. A. (2002). A comparison of methods for monitoring multitemporal vegetation change using Thematic Mapper imagery. *Remote Sensing of Environment*, 80, 143–156.
- Small, C. (2001). Multiresolution analysis of urban reflectance. *Remote sensing data fusion over urban areas, IEEE/ISPRS Joint Workshop 2001 IEEE, Rome, Italy* (pp. 15–19).
- Small, C. (2002). Multitemporal analysis of urban reflectance. *Remote Sensing of Environment*, 81, 427–442.
- Smith, M. O., Johnson, P. E., & Adams, J. B. (1985). Quantitative determination of mineral types and abundances from reflectance spectra using principal components analysis. *Journal of Geophysical Research*, 90, C797–C804.
- Theseira, M. A., Thomas, G., & Sannier, C. A. D. (2002). An evaluation of spectral mixture modelling applied to a semi-arid environment. *International Journal of Remote Sensing*, 23, 687–700.
- Tompkins, S., Mustard, J. F., Pieters, C. M., & Forsyth, D. W. (1997). Optimization of endmembers for spectral mixture analysis. *Remote Sensing of Environment*, 59, 472–489.